*Chem. Mater.* **2008,** *20,* 4783–4790

# Three-Dimensionally Ordered Macroporous Lithium Manganese Oxide for Rechargeable Lithium Batteries

Dino Tonti,*,† María José Torralvo,‡ Eduardo Enciso,§ Isabel Sobrados,† and Jesus Sanz†

*Instituto de Ciencia de Materiales de Madrid, Consejo Superior de Investigaciones Científicas (CSIC), C/Sor Juana Inés de la Cruz, 3, ES 28049 Madrid, Spain, Departamento de Química Inorgánica I, Facultad de Ciencias Químicas, Universidad Complutense de Madrid, Ciudad Universitaria, ES 28040 Madrid, Spain, and Departamento de Química-Física I, Facultad de Ciencias Químicas, Universidad Complutense de Madrid, Ciudad Universitaria, ES 28040 Madrid, Spain*

*Received July 31, 2007. Revised Manuscript Received May 7, 2008*

Three-dimensionally ordered macroporous (3DOM) $LiMn_2O_4$ spinel was prepared by a colloidal templating process. An opal structure consisting of monodispersed poly[styrene-*co*-methacrilic acid] beads (380 nm in diameter) was used as a template. After infiltration of Li and Mn nitrates, the assembly was calcined in air at temperatures between 500 and 700 °C. Chemical processes were studied by means of thermal analysis, X-ray diffraction (XRD), and solid-state nuclear magnetic resonance (NMR). Morphological and microstructural characterizations were carried out by scanning and transmission electron microscopy (SEM, TEM) and by gas adsorption volumetry. Despite the simple preparation procedure, several steps are detected, which prove to be critical for the successful formation of high-quality 3DOM materials. Optimization of the preparation conditions gave extended macroporous networks with relatively smooth nanocrystalline spinel walls and a surface area of 24 $m^2$/g. Porosity results from three ranges of pores: (1) the macroporous sublattice (replica of the opal lattice), (2) the pores formed after mineralization of the tetrahedral and octahedral holes of the template, and (3) the porosity from the nanocrystallites forming roughened macroporous walls. Films of 3DOM $LiMn_2O_4$ were prepared on conductive substrates and used as electrodes, showing fast and reversible lithium deinsertion over a large number of cycles without suffering significant morphological or electrochemical degradation.

## Introduction

Many applications are demanding lithium batteries with higher power than currently available. Higher current rates can be achieved with three-dimensionally (3D) nanostructured electrodes.[1] Lithium can be readily intercalated and deintercalated into submicrometric particles, as a consequence of the short diffusion paths. The increased surface area ensures locally lower current densities, which allows higher charge−discharge rates without capacity loss. A three-dimensional particle connectivity is the one that best preserves the advantage of short diffusion paths with high surface area, offering in addition structural stability. Much research has focused to prepare nanostructured electrodes and to investigate their electrochemical lithium intercalation.[2–7] Among these, three-dimensional periodically ordered macroporous (3DOM) structures offer an optimal morphology, as they provide submicrometric particles fused in a skeleton that is readily and uniformly accessible to the electrolyte. Contrary to conventional pressed powders, this structure provides a continuous pathway for ionic and electronic conduction with low angle grain boundaries, which reduces polarization and minimizes grain–grain interface problems.[8–12] As a consequence of both grain connectivity and 3D structure, millimeter-thick electrodes can be prepared.[13] Ordered macroporous carbon showed significantly higher capacitance at high discharge than did conventional carbon-based anodes for battery applications.[13] Several ordered macroporous oxides, including $LiCoO_2$,[14] $V_2O_5$, $LiNiO_2$,[15] $SnO_2$,[16] $Li_4Ti_5O_{12}$,[12,17]

---

* Corresponding author. Phone: +34-913349026. Fax: +34-913720623. E-mail: dino@icmm.csic.es.

† CSIC.

‡ Departamento de Química Inorgánica I, Universidad Complutense de Madrid.

§ Departamento de Química-Física I, Universidad Complutense de Madrid.

(1) Long, J. W.; Dunn, B.; Rolison, D. R.; White, H. S. *Chem. Rev.* **2004**, *104*, 4463.
(2) Nishizawa, M.; Mukai, K.; Kuwabata, S.; Martin, C. R.; Yoneyama, H. *J. Electrochem. Soc.* **1997**, *144*, 1923.
(3) Coustier, F.; Passerini, S.; Smyrl, W. H. *J. Electrochem. Soc.* **1998**, *145*, L73.
(4) Arico, A. S.; Bruce, P.; Scrosati, B.; Tarascon, J.-M.; Van Schalkwijk, W. *Nat. Mater.* **2005**, *4*, 366.
(5) Curtis, C. J.; Wang, J. X.; Schulz, D. L. *J. Electrochem. Soc.* **2004**, *151*, A590.
(6) Suzuki, N.; Sasaki, H.; Morinaga, Y.; Yamada, Y. *Appl. Surf. Sci.* **2005**, *252*, 1498.
(7) Bing, Z.; Yuan, Y.; Wang, Y.; Fu, Z. W. *Electrochem. Solid-State Lett.* **2006**, *9*, A101.
(8) Nishizawa, M.; Hashitani, R.; Itoh, T.; Matsue, T.; Uchida, I. *Electrochem. Solid-State Lett.* **1998**, *1*, 10.
(9) Arora, P.; Doyle, M.; Gozdz, A. S.; White, R. E.; Newman, J. *J. Power Sources* **2000**, *88*, 219.
(10) Meyers, J. P.; Doyle, M.; Darling, R. M.; Newman, J. *J. Electrochem. Soc.* **2000**, *147*, 2930.
(11) Bard, A. J.; Faulkner, L. R. *Electrochemical Methods: Fundamentals and Applications*, 2nd ed.; John Wiley and Sons: New York, 2000.
(12) Sorensen, E. M.; Barry, S. J.; Jung, H. K.; Rondinelli, J. R.; Vaughey, J. T.; Poeppelmeier, K. R. *Chem. Mater.* **2006**, *18*, 482.
(13) Lee, K. T.; Lytle, J. C.; Ergang, N. S.; Oh, S. M.; Stein, A. *Adv. Funct. Mater.* **2005**, *15*, 547.
(14) Ergang, N. S.; Lytle, J. C.; Yan, H. W.; Stein, A. *J. Electrochem. Soc.* **2005**, *152*, A1989.
(15) Yan, H. W.; Sokolov, S.; Lytle, J. C.; Stein, A.; Zhang, F.; Smyrl, W. H. *J. Electrochem. Soc.* **2003**, *150*, A1102.

10.1021/cm702134s CCC: $40.75

that have been prepared via colloidal crystal templating methods are interesting insertion materials as either cathodes or anodes in lithium-ion cells.

3DOM materials can be prepared by template-based methods using opals, that is, arrays of monodisperse spherical colloidal particles.[18] Void spaces between particles are filled with fluid precursors that are converted to a solid before removal of the template material. If the template material is a polymer, often the templated inverse opal (a 3DOM structure) is obtained with a simple heating ramp. It has been possible to prepare 3DOM carbon monoliths of lateral sizes of the order of 1 cm, which could be handled and directly used as active electrodes.[13] Instead, oxides usually present severe mechanical problems during and after their preparation, such as crystallite coarsening, strains, and fractures, which affect the wall regularity and the long-range integrity. Typically, fragments of less than 1 mm are obtained, a fact that limits the practical interest of these materials, because additives such as binders and conducting agents are necessary for their assembly as electrode, just as conventional powders.

$LiMn_2O_4$ has been extensively investigated for decades because with a theoretical energy density comparable to that of $LiCoO_2$ used commercially, it can be prepared by soft chemistry methods with low cost and toxicity.[19] In this Article, we present a study of the template formation of 3DOM lithium manganese oxides from impregnated salts in a latex opal. Despite the interest for this material, to the best of our knowledge, reports on its preparation as 3DOM material are scarce.[20] We found that the possibility to obtain a 3DOM $LiMn_2O_4$ critically depended on the salt used and the thermal treatment; therefore, particular emphasis was given to the understanding of the formation process. A well-defined sequence of steps is necessary for the successful formation of the inverse opal. We managed to separate these steps and obtain both monoliths with sizes of several millimeters and films directly on current collectors. The latter were used without assistance of additives for electrochemical tests, which reproduced the typical behavior described for conventional $LiMn_2O_4$ with excellent rate capability and good capacity retention over multiple cycles, showing the possible utilization of prepared materials as cathode of Li-ion batteries.

## Experimental Section

**Synthesis of Latex Particles and Preparation of the Latex Arrays.** Spherical latex particles (diameter of 380 nm) were prepared by a copolymerization reaction of styrene and methacrylic acid in a surfactant-free emulsion as described in detail earlier.[21] The product, poly[styrene-*co*-methacrylic acid] (PS-MAA), was dialyzed against water prior to use. From the particle suspensions, latex opals were prepared by evaporating the solvent at 40 °C. Monoliths were collected at the bottom of the beaker; in the case of films, the opal assembled on the surface of a gold-sputtered (12 min at 20 mA) 10 × 20 mm vertically suspended alumina plate (CoorsTek). An ethanolic 1.3 M $LiNO_3$ 2.6 M $Mn(NO_3)_2 \cdot 4H_2O$ solution was infiltrated in the free voids of the latex array. For comparison, a latex opal was infiltrated with a 2 M Mn(II) acetate and 1 M Li nitrate water/ethanol 2:1 (w/w) solution. The composite material template/inorganic precursor was kept at room temperature for 24 h in a dry atmosphere and heated in static air with a 0.5 °C/min rate to a final temperature of either 500 or 700 °C and was kept at this temperature for 3 h. During thermal treatment the template is eliminated, and Li, Mn oxide spinel is obtained.

**Characterization Techniques.** Structural characterization of the inorganic materials was made by X-ray (XRD) and selected area electron diffraction (SAED). XRD diagrams were recorded in a Bruker D8 Advance powder diffractometer using Cu Kα radiation. Crystallographic phases were matched with reference XRD patterns using PCPDFWIN V.2.2, and relative amounts were roughly estimated through simulation of XRD patterns with the PowderCell 2.4 program.[22]

SAED patterns were obtained in a JEOL 2000 FX electron microscope equipped with a double tilting (±45°) sample holder, operating at 200 kV. Transmission electron microscopy (TEM) was also used to characterize the mean size of the latex particles and the morphology and microstructure of inorganic porous materials. In this analysis, a JEOL-JEM 3000F electron microscope operating at 300 kV was used. In each case, the sample was suspended in butanol and a drop of the suspension was deposited over a copper grid coated with a holey carbon support film. The inorganic porous samples and the latex particles arrays were also characterized by scanning electron microscopy (SEM) and by $N_2$ adsorption at 77 K. Samples for SEM were deposited on a metallic support and coated with a gold film before observation in a JEOL 6400 electron microscope operating at 20 kV. The adsorption−desorption measurements were made in an ASAP 2020 Micromeritis equipment. Prior to the adsorption experiments, the samples were outgassed at 110 °C for 3 h. The isotherms were analyzed using the BET model with 0.162 $nm^2$ as the molecular cross-sectional area for adsorbed nitrogen.[23] The pore size distributions were obtained by the BJH method[24] using the Kelvin equation with the assumption of cylindrical pores.[25]

Differential thermal analysis (DTA) and thermogravimetric (TGA) curves were recorded simultaneously on impregnated opals in a Seiko 320U instrument. The temperatures were measured with an accuracy of ±1 °C. Analyses were carried out in a 100 mL/min air flux. The sample and reference were placed in platinum crucibles, and $\alpha$-$Al_2O_3$ was used as inert reference. The qualitative determination of gases evolved during the thermal treatment was done by mass spectrometry with a Thermostar quadrupole mass spectrometer coupled to the TG/DTA instrument. Argon was used as the gas carrier, with a flux of 200 mL/min.

$^7$Li NMR spectra were recorded at room temperature in an AVANCE-400 Bruker spectrometer. The frequency used was 155.50 MHz (9.4 T). Spectra were obtained after single pulse irradiation (3 $\mu$s) with a recycling time of 10 s. Samples were spun at 10 kHz around an axis inclined at 54°44′ with respect to the magnetic field (magic-angle spinning technique, MAS). In all experiments, the number of scans was fixed to 200. $^7$Li chemical

---

(16) Lytle, J. C.; Yan, H. W.; Ergang, N. S.; Smyrl, W. H.; Stein, A. *J. Mater. Chem.* **2004**, *14*, 1616.

(17) Woo, S. W.; Dokko, K.; Kanamura, K. *Electrochim. Acta* **2007**, *53*, 79.

(18) Velev, O. D.; Lenhoff, A. M. *Curr. Opin. Colloid Interface Sci.* **2000**, *5*, 56.

(19) Amatucci, G.; Tarascon, J. M. *J. Electrochem. Soc.* **2002**, *149*, K31.

(20) Song, C. X.; Yang, L. X.; Chen, X. M.; Wu, S. Y.; Wang, X. Y. *Chem. J. Chin. Univ.* **2007**, *28*, 204.

(21) Carbajo, M. C.; Lopez, C.; Gomez, A.; Enciso, E.; Torralvo, M. J. *J. Mater. Chem.* **2003**, *13*, 2311.

(22) Kraus, W.; Nolze, G. *J. Appl. Crystallogr.* **1996**, *29*, 301.

(23) Rouquerol, F.; Rouquerol, J.; Sing, K. *Adsorption by Powders and Porous Solids*; Academic Press: London, 1999.

(24) Barret, E. P.; Joyner, L. G.; Halenda, P. P. *J. Am. Chem. Soc.* **1951**, *73*, 373.

(25) Broekhof, J. C.; Deboer, J. H. *J. Catal.* **1968**, *10*, 368.

shift values were given relative to a 1 M LiCl solution. Fitting of MAS NMR spectra was carried out with the Bruker WINFIT software package. This program allows the spinning rate and the position, line width, and intensity of components to be determined with a nonlinear least-squares interactive method. To preserve the quantitative analysis, no mathematical treatment of NMR signals was used.

For electrochemical measurements, inverse opal films prepared over a metallized alumina plate were used. A three-electrode cell was assembled using a commercial Ag/AgCl reference electrode (Crison) and a Pt foil as counter-electrode, and a saturated (~9 M) Li nitrate aqueous solution as electrolyte. For an easier comparison with experiments in organic electrolyte, the voltage was referred to the $Li^+$/Li pair by adding to the measured value the potential 3.25 V of our Ag/AgCl reference electrode vs the $Li^+$/Li potential.[26–28] Cycling voltammetry experiments were conducted using an EG&G Princeton Applied Research model 273A potentiostat/galvanostat. The current response was filtered with a 5.3 Hz low pass filter. For galvanostatic cycling studies, a Solartron Multistat 1480 multipotentiostat was used.

## Results and Discussion

**Thermal Processing of Impregnated Opals.** The shape transfer from the organic template to the inverse inorganic phase requires a sequence of chemical or physical steps that appropriately change the state and the mechanical properties of both phases initially present in the impregnated opal composite. This holds for any method used to induce such transformations, in our case a simple thermal treatment in air. It is well-known that polystyrene and its copolymers undergo a glass transition at about 95 °C, and in air start decomposing at 250 °C. In this temperature range, the polymer is in a fluid state: if the templated precursor phase is also liquid, molding becomes problematic, as the interface will depend on fluidities and liquid−liquid interactions. To prevent a fully liquid state, the consolidation of the molded phase must occur at a temperature below the polymer glass transition. Further solid-state chemical steps may then be produced, as long as they do not affect the shapes obtained.

$Mn(NO_3)_2$ has been used as precursor by Martin and coworkers for the template preparation of $LiMn_2O_4$ nanotubules.[28] In our case, Mn(II) nitrate was also used to obtain inverse opals. If instead of the nitrate the acetate was used, the shape transfer failed, and only a thinner, microscopically irregular porous solid was found, resulting from the collapse of the opal structure and the subsequent mixing of polymer and inorganic precursor. This may result in phenomena similar to those occurring during a Pechini synthesis,[29] where precursor cations are chelated by a polymer, intimately mixing the forming inorganic phase with the decomposing organic phase.

To understand and control changes produced by heating, we have (a) thermally analyzed the opal impregnated with Li and Mn nitrate solution and (b) studied by XRD and NMR the formation of $LiMn_2O_4$ from nitrate solution without latex.

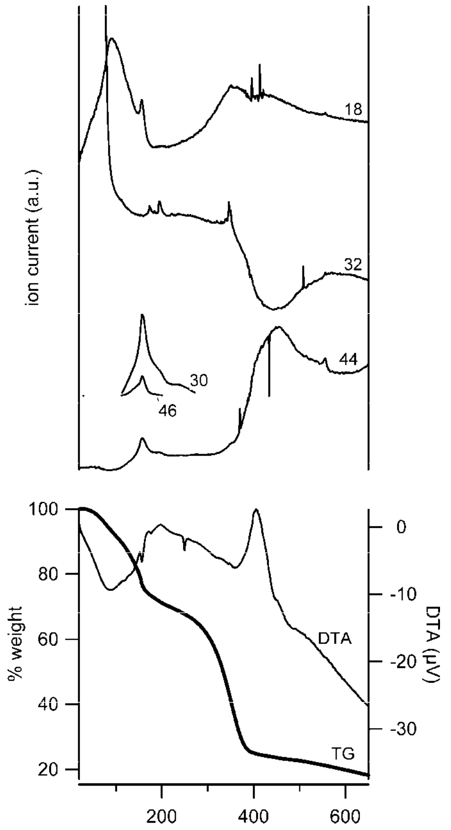

**Figure 1.** TG/DTA (bottom) and mass curves (top) recorded simultaneously for impregnated opals at heating rates of 5 °C/min under Ar flow. Numbers indicate the *m*/*z* values for each trace. We assign these values to the following species: $H_2O$ (18), NO (30), $O_2$ (32), $CO_2$ (44), $NO_2$ (46).

Thermal analysis, combining gravimetric, differential analysis, and mass spectroscopy, is reported in Figure 1. To couple the quadrupole mass spectrometer to the experiment, it is necessary to use an inert transport gas. In these experiments, the sample is placed in an argon flow, and therefore the environment is poorer in oxygen than during oven calcination. Nevertheless, TG curves in argon and air flow compare well (see Supporting Information S1). Under argon flow, using ramps between 1 and 10 °C/min, results are qualitatively similar. Mass weight was lost above 100 °C. In the range 100−200 °C, a mass *m*/*z* of 18 amu ($H_2O$) is detected, which is consistent with the broad endothermic peak visible in DTA: water is slowly eliminated from reprecipitated $Mn(NO_3)_2 \cdot xH_2O$. In these conditions, without a rigid wall the polymer would collapse; air or low viscosity fluids would be expulsed from the voids, and opals kept at 120 °C become transparent after a few minutes. Starting from 150 °C, a finer structure of endothermic peaks appears in DTA; masses of 30 (NO) and 46 ($NO_2$) clearly indicate nitrate decomposition. This corresponds to the decomposition of $Mn(NO_3)_2$; its temperature is reported in literature around 200 °C in the pure state, lower if the salt is mixed with an inert powder such as acetylene black.[30] $LiNO_3$ does not decompose at this stage. The sharp endothermic peak at 250 °C is not associated with any weight loss and can be attributed to $LiNO_3$ melting.[31]

Above 350 °C, the oxygen depletion (*m*/*z* 32), the rise of $CO_2$ concentration (*m*/*z* 44), and the endothermic peak indicate the polymer decomposition. In air, this process is

---

(26) Li, W.; McKinnon, W. R.; Dahn, J. R. *J. Electrochem. Soc.* **1994**, *141*, 2310.

(27) Lee, J. W.; Pyun, S. I. *Electrochim. Acta* **2004**, *49*, 753.

(28) Li, N.; Patrissi, C. J.; Che, G.; Martin, C. R. *J. Electrochem. Soc.* **2000**, *147*, 2044.

(29) Liu, W.; Farrington, G. C.; Chaput, F.; Dunn, B. *J. Electrochem. Soc.* **1996**, *143*, 879.

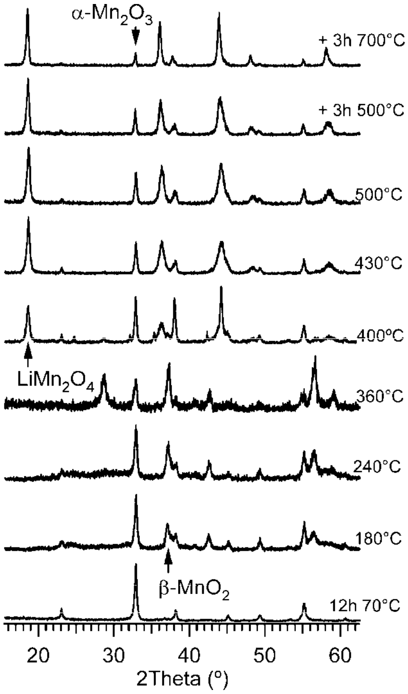

**Figure 2.** XRD patterns of samples heated at increasing temperatures. The bottom trace corresponds to the powder filtered from a $LiNO_3/Mn(NO_3)_2$/EtOH mixture (no template present). Next traces are marked with temperatures corresponding to the stopping points of heating ramps (1 °C/min) of mixtures with the same composition. Top two traces correspond to inverse opal formed after the same ramp, with additional treatment at 500 and 700 °C. Spectra were normalized relative to the strongest intensity; arrows point to the most intense line of each phase.

more vigorous, as deduced from DTA curves where a widely exothermal balance starts already at 200 °C (see Supporting Information S1). In air, if the heating rate is faster than 1 °C/min, sudden mass decays accompanied by bursts of strong heat release are produced, which indicate combustion. Such events should be avoided, as they imply inhomogeneous overheating and violent gas release. In such cases, polymer removal can even be delayed to temperatures of about 450 °C, probably due to coke formation, which is more difficult to remove. Above 500 °C, weight changes and heat releases are minor, although persistent $CO_2$ emission indicates that complete elimination of polymer-derived products is lengthy.

Solid-state reactions leading to lithiated manganese oxide were followed by stopping at increasing temperatures the heating ramp of the precursor solution. Heating a $Mn(NO_3)_2$ water or ethanol solution at 70 °C produces a black slurry that even after several hours does not dry out. A black precipitate can be isolated by washing it with the solvent. XRD indicates that the powder is purely $\alpha$-$Mn_2O_3$ (Figure 2, bottom spectrum). The same reaction was detected in air at ordinary or at 90 mmHg pressure, but no reaction was seen when $Mn(NO_3)_2$ was changed with $MnCl_2$. Therefore, we infer an oxidation carried out not by atmospheric oxygen, but rather by $NO_3^-$ anions:

$$2Mn^{2+} + 2NO_3^- + H_2O \rightarrow Mn_2O_3 + 2NO_2 + 2H^+ \quad (1)$$

Water is provided by the Mn nitrate salt, which is commercially available as tetrahydrate. Formation of $Mn_2O_3$ at low temperature from part of Mn nitrate is a key step that was not observed with Mn acetate opal impregnation. This oxide probably precipitates on the surface of the PS beads, building a rigid cage that retains its shape when, at higher temperature, the polymer becomes fluid. All described processes are produced without participation of $LiNO_3$. This compound can be observed as cubic crystals or detected by XRD in dried samples; however, it can be dissolved by atmospheric moisture within a few hours.

XRD data (Figure 2) at 180 and 240 °C show increasing quantities of $\beta$-$MnO_2$ (rutile structure). This should be the product of the second nitrate decomposition (150−200 °C, see thermal analysis above), which eliminates the residual $Mn(NO_3)_2$:

$$Mn(NO_3)_2 \rightarrow MnO_2 + 2NO_2 \quad (2)$$

The balance between $Mn_2O_3$ and $MnO_2$ shifts in favor of the latter at 360 °C. This oxidation can be produced by oxygen:

$$Mn_2O_3 + 1/2O_2 \rightarrow 2MnO_2 \quad (3)$$

Following the XRD results, at nearly 400 °C a spinel $LiMn_2O_4$ phase forms while $MnO_2$ disappears completely. This result can be explained by a reaction with $LiNO_3$ (the presence of $NO_3^-$ ions in the 360 °C sample was confirmed by infrared spectroscopy):

$$2MnO_2 + LiNO_3 \rightarrow LiMn_2O_4 + NO_2 + 1/2O_2 \quad (4)$$

The structure of $\beta$-$MnO_2$ is different from that of the resulting $LiMn_2O_4$ spinel; however, David et al. have proposed a mechanism involving the topotactic insertion of $Li^+$ ions and the subsequent cooperative jump of Mn ions to neighbor sites.[32] This mechanism permits a phase transformation without major morphological change. Thus, the inverse opal structure is retained thanks to both $Mn_2O_3$ preserving the template shape during polymer softening and elimination, and $MnO_2$ able to transform into the final spinel compound without affecting its crystallite shape and arrangement.

The residual $Mn_2O_3$ phase is progressively converted into the more stable $LiMn_2O_4$, but this process requires higher temperatures and longer times. A structural analysis indicates the existence of about 10% $Mn_2O_3$ after 3 h treatment at 700 °C.

Reaction between $LiNO_3$ and manganese oxide can be considered a form of the lithium impregnation method,[33] which was introduced to maximize the contact surface between the lithium and the manganese sources: holding the temperature at 270 °C lithium fills the pores of the oxide powder, determining a lower temperature and a higher quality of the spinel if compared to other solid-state methods. Even lower formation temperatures have been reported with methods favoring atomic level intermixing between lithium and manganese salts. If metal ions are coordinated by carboxylates, $LiMn_2O_4$ starts forming directly at ~250 °C, with no intermediate formation of manganese oxides.[29,34–40] For our purposes, early formation of $Mn_2O_3$ is a critical step,

---

(30) Tang, W.; Yang, X.; Liu, Z.; Ooi, K. *J. Mater. Chem.* **2003**, *13*, 2989.
(31) Fey, G. T. K.; Cho, Y. D.; Kumar, T. P. *Mater. Chem. Phys.* **2006**, *99*, 451.
(32) David, W. I. F.; Thackeray, M. M.; Bruce, P. G.; Goodenough, J. B. *Mater. Res. Bull.* **1984**, *19*, 99.
(33) Xia, Y.; Yoshio, M. *J. Electrochem. Soc.* **1996**, *143*, 825.

while formation of a solid product at 250 °C could not lead to the template morphology. We believe this is the main difference between nitrates and acetates in producing the 3DOM structure. A general study pointing out the importance of a metal oxide formation prior to the template glass transition temperature has appeared during the reviewing process of this manuscript.[41] The authors suggest the nitrate oxidation as a general route for the preparation of a wide range of simple and mixed oxides.

The phase transformation also produces changes in the lithium chemical environment. $^7$Li ($I = 3/2$) MAS NMR spectra of $LiNO_3$ infiltrated opals are formed by one component centered at 0 ppm (Figure 3). In this sample, the partial cancelation of dipolar and quadrupolar interactions improved experimental resolution, showing the presence of a single component. During formation of $MnO_2$, $^7$Li signal has a 0 ppm shift and is symmetrically broadened. We attribute the absence of XRD patterns ascribed to crystalline Li compounds to their hydrated state (see above). After reaction of $MnO_2$ with Li, the 0 ppm phase disappears, and the NMR spectrum is constituted by two components at ~100 and 500 ppm (Figure 3). The 100 ppm component is broad and asymmetric and is most likely related to formation of paramagnetic (non-closed electronic orbitals) Mn compounds. The magnitude of this shift implies a short Mn−Li distance, as it could be the case for adsorbed Li species. However, the large amount of lithium present in this state suggests that it is rather an amorphous compound. The symmetric component detected at 500 ppm, ascribed in previous works to $LiMn_2O_4$,[42] indicates the formation of spinel. This must be at expenses of the amorphous phase; in fact, in samples heated for longer time at 500 °C the 100 ppm component disappears, and $^7$Li NMR spectra are formed by two broad symmetric components at 500 and 1500 ppm, ascribed to tetra and octahedral Li in $LiMn_2O_4$ spinel. In both cases, chemical shift values are produced by the Fermi contact interaction, which changes the impaired electron density transferred from the paramagnetic center to Li ions.[42] The octahedral component is not detected in samples heated above 600 °C. In samples calcined at increasing temperatures, the crystallinity of $LiMn_2O_4$ increases, decreasing the line width of spinning sidebands.

**Microstructural Characterization.** Micrographs of Figures 4 and 5 show the inorganic framework that encloses the porous system formed when the template is eliminated.

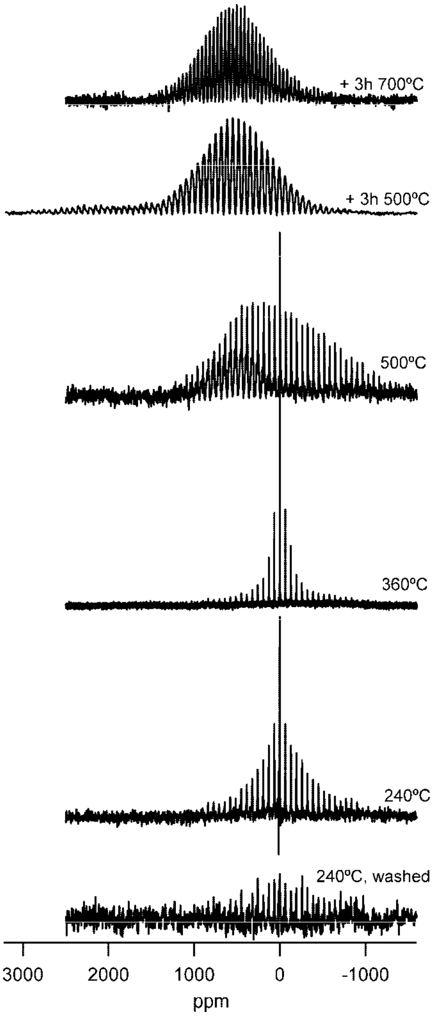

**Figure 3.** $^7$Li MAS NMR spectra recorded at room temperature on samples obtained at increasing temperatures. The bottom trace corresponds to a sample obtained from a $LiNO_3/Mn(NO_3)_2$/EtOH mixture (no template present) heated to 240 °C at 1 °C/min and subsequently washed with ethanol. Next traces are marked with temperatures corresponding to the stopping points of 1 °C/min heating ramps of mixtures with the same composition, without washing. Top two traces correspond to inverse opal formed after the same ramp, with additional treatment of 3 h at 500 and 700 °C.

The SEM image of Figure 4a shows the ordered hollow spheres that form the macroporous face centered cubic (fcc) lattice replica of the latex opal and the large circular interconnecting windows (LW) at the positions corresponding to the contact points of contiguous latex particles of the template (darker areas). The space between nearest macropores that corresponds to tetrahedral (Th) and octahedral (Oh) holes in the template is occupied by the oxide and appears as clearer areas. Image **4a** corresponds to a commonly found [111] surface, but occasionally different surfaces, such as the [100] (**4b**), can also be observed. The opal assembling process usually starts by packing spheres at the surface of the latex suspension. The hexagonal symmetry is the most compact 2D arrangement; however, other arrangements can also kinetically form.

In Figure 5a, the TEM image shows the octahedral and tetrahedral holes projected in the [100] direction (hence the same symmetry is observed as in Figure 4b). These cavities appear partially mineralized, with the inorganic material forming a wall around the hollow spheres and creating

---

(34) Sun, Y.-K.; Kim, D.-W.; Choi, Y.-M. *J. Power Sources* **1999**, *79*, 231.
(35) Hon, Y. M.; Fung, K. Z.; Lin, S. P.; Hon, M. H. *J. Solid State Chem.* **2002**, *163*, 231.
(36) Barboux, P.; Tarascon, J. M.; Shokoohi, F. K. *J. Solid State Chem.* **1991**, *94*, 185.
(37) Lee, Y.-S.; Sun, Y.-K.; Nahm, K.-S. *Solid State Ionics* **1998**, *109*, 285.
(38) Prabaharan, S. R. S.; Saparil, N. B.; Michael, S. S.; Massot, M.; Julien, C. *Solid State Ionics* **1998**, *112*, 25.
(39) Kang, H. K.; Ahn, W.; Lee, S. G.; Han, K. S.; Song, J. H.; Kwon, O. H.; Kang, E. Y. *J. Power Sources* **2006**, *163*, 166.
(40) Takada, T.; Enoki, H.; Hayakawa, H.; Akiba, E. *J. Solid State Chem.* **1998**, *139*, 290.
(41) Sadakane, M.; Horiuchi, T.; Kato, N.; Takahashi, C.; Ueda, W. *Chem. Mater.* **2007**, *19*, 5779.
(42) Lee, Y. J.; Wang, F.; Grey, C. P. *J. Am. Chem. Soc.* **1998**, *120*, 12601.

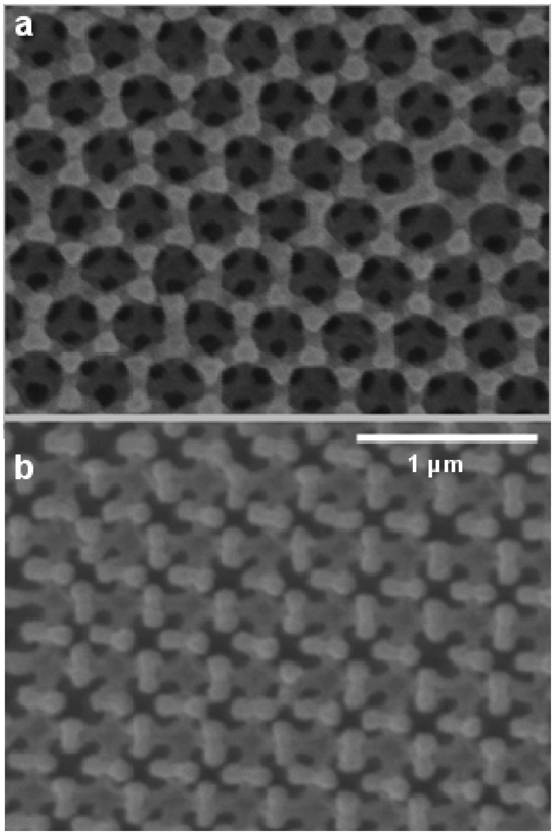

**Figure 4.** SEM micrographs of 3DOM $LiMn_2O_4$. Images a and b correspond to [111] and [100] surfaces, respectively.

porosity inside the inorganic framework. XRD and SAED (not shown) patterns are similar to those obtained from calcination of the solution and indicate that the inorganic framework is prevalently made of $LiMn_2O_4$ nanocrystals with about 10% $Mn_2O_3$ impurity.

Micrographs of Figure 5 show the microstructure of the inorganic skeleton. Images **5a** and **5b** correspond to the fcc lattice of macropores projected in a direction close to [110] and show the macropore walls of consecutive layers with the partially occupied tetrahedral and octahedral holes not completely aligned. The mean size (major dimension) of the nanocrystals, measured from the images, ranges from 5 to 20 nm. From the TEM micrographs, the mean diameter of macropores (355 nm) and the macropore wall thickness (8–12 nm) have been estimated. From the difference of the distance between the particle center-to-center in the template and the distance between the macropore centers, a structural contraction of less than 2% has been calculated. This reduced contraction minimizes strains and contributes to the macroscopic stability of the structure, which favored the preparation of large monolithic plates that reached sizes of the order of 1 × 10 × 10 mm. The cross section of a completely molded monolith is presented in Figure 6. In the Supporting Information (S2), large-scale images are reported where macroporosity can be appreciated.

This macroporous material presents a nitrogen adsorption isotherm of type IV, which is usually associated with mesopores with hysteresis loop of type H1. The BET area calculated from the isotherm (24 $m^2/g$) is larger than the area calculated for the inverse opal geometry (8 $m^2/g$), but very small as compared to the sum given by all individual crystallites (about 100 $m^2/g$ for $LiMn_2O_4$ nanocrystals of dimensions 20 nm × 20 nm × 10 nm). These results suggest that nanocrystals must be closely packed and/or sintered and that the difference between the experimental and the calculated value of the surface corresponds to the porosity inside the inverse opal skeleton (see Figures 4 and 5). As deduced from the images, in addition to (1) the pores (hollow spheres) left by the template, further contributions are (2) the pores left after mineralization inside the tetrahedral and octahedral holes of the template and (3) the grain–grain interstices and wall roughness. Three orders of porosity have been found also in other 3DOM materials.[43]

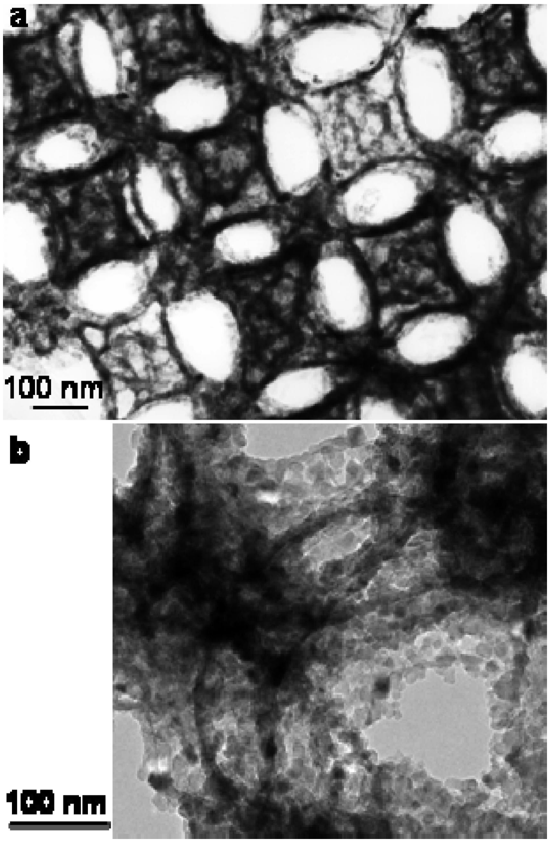

**Figure 5.** TEM micrographs showing the macropore walls formed by $LiMn_2O_4$ nanocrystals. The images correspond to projections of 3DOM $LiMn_2O_4$ inverse opals close to [100] (a) and [110] (b) directions.

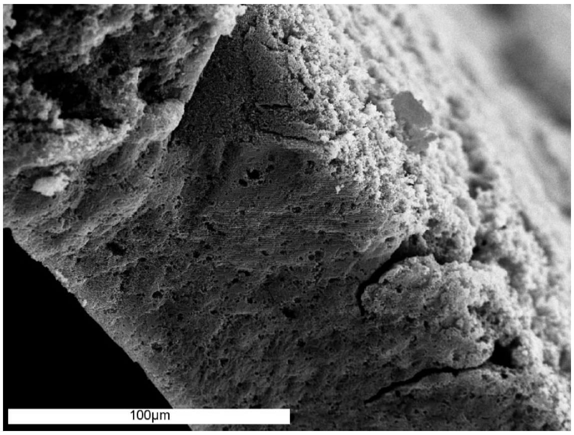

**Figure 6.** SEM micrograph of a typical monolith of inverse opal $LiMn_2O_4$.

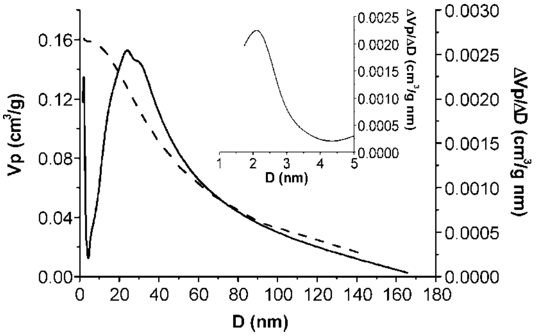

**Figure 7.** Desorption-based pore size distribution (–) and cumulative pore volume (– – –) corresponding to a 3DOM $LiMn_2O_4$ sample. The inset shows an expansion of the pore size distribution curve in the 1−5 nm region.

We analyzed porosity by nitrogen absorption. No significant condensation seems to occur in the macropores during adsorption as indicated by both the pore size distribution and the cumulative pore volume (not shown). Figure 7 shows the cumulative pore volume and the pore size distribution obtained from desorption data. During desorption the condensate evaporates from the pore entrances, whose size determines the positions of maxima in the size distribution. Most of the condensate evaporates through pore openings with diameter ranging from 10 to 60 nm. This matches the size expected for openings on the partially filled Th and Oh; therefore, it can be assigned to porosity (2). The maximum at about 2 nm can be assigned to the wall roughness due to the nanometer-sized crystallites, thus to contribution 3. As indicated by the pore volume trace, its volume is very small as compared to that of porosity (2).

**Electrochemical Activity.** For the electrochemical study, thin 3DOM electrodes were deposited on gold-coated alumina plates, on a surface of approximately 1 cm$^2$. This has the advantage of a more direct evaluation of the 3DOM structure, as no further processing of the active material is required, such as grinding or using additives (binders or electronic conductors). To avoid an excess of precursors that may eventually cover the macroporous structure with crusts, only the amount of nitrate solution required for the opal layer wetting was used. This resulted in a smaller nitrate/opal ratio, and contraction was larger than usually observed in monoliths. When prepared in thin layer, shrinkage of the inorganic framework during calcination produced islands of inverse opals of lateral size of tens of micrometers, as illustrated in Figure 8. Their thickness is typically of the order of 20 hollow spheres, about 5 $\mu$m. Despite the contraction, adhesion on the substrate is excellent, as witnessed by the trace of the first opal layer left on the alumina region that remains uncovered when cracks develop (see, for instance, the right side of Figure 8).

To evaluate intrinsic effects of electrochemical cycling on the macroporous structure and on its adhesion to the substrate, we did not use organic solvents, which may leave decomposition residuals masking the electrode morphology, as in the case reported by Lytle et al.[16] $LiMn_2O_4$ electrodes cycled in aqueous electrolyte in the 3 and 4 V potential region[2,26,44–46] are reported to produce results very close to those usually observed with organic solvents.[27,47] In addition, with aqueous electrolytes the ionic conductivity is higher than that with organic electrolytes, which allows the electrochemical study at high rates, without problems associated with ohmic losses.[27,46]

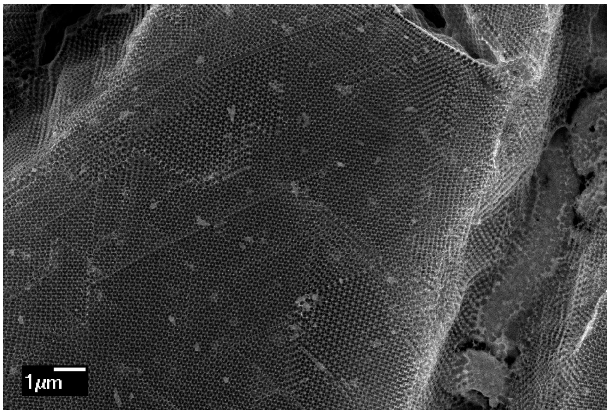

**Figure 8.** SEM micrograph of a layer of 3DOM $LiMn_2O_4$ prepared on an alumina plate.

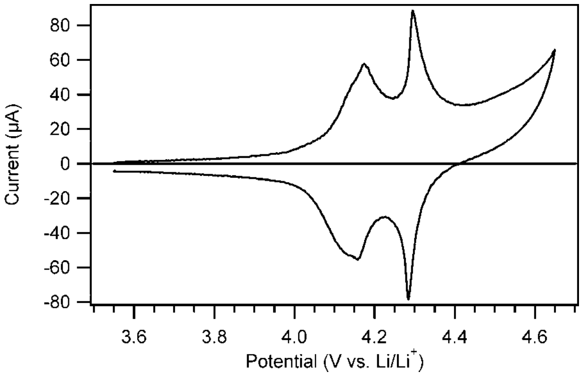

**Figure 9.** First-scan cyclic voltammogram of 3DOM lithium manganese oxide electrodes in a 9 M $LiNO_3$ aqueous solution. Scan speed 0.5 mV/s.

A typical cyclic voltammogram is reported in Figure 9, showing reversible peaks at 4.1 and 4.3 V vs Li/Li$^+$. These values are in good agreement with those reported by Li et al.[28] They correspond to the sequential intercalations:

$$1/2\mathrm{Li} + \mathrm{Mn_2O_4} \rightarrow \mathrm{Li_{1/2}Mn_2O_4} \tag{5}$$

$$1/2\mathrm{Li} + \mathrm{Li_{1/2}Mn_2O_4} \rightarrow \mathrm{LiMn_2O_4} \tag{6}$$

The very small peak separation (10−20 mV at a scan rate of 0.5 mV/s) indicates finite Li diffusion in the thickness of active material (10−20 nm), an effect that with submicrometric particles is only obtained at 10 times slower scan rates.[28] The anodic current in the region above 4.4 V probably corresponds to water oxidation. Given the high surface to volume ratio of the sample, this contribution as compared to the insertion–deinsertion effects is relatively large. Thin films prepared without template showed a much smaller current in the same region. For this reason,

---

(43) Carbajo, M. C.; Enciso, E.; Torralvo, M. J. *Colloids Surf., A* **2007**, *293*, 72.

(44) Li, W.; Dahn, J. R. *J. Electrochem. Soc.* **1995**, *142*, 1742.

(45) Li, W.; Dahn, J. R.; Wainwright, D. S. *Science* **1994**, *264*, 1115.

(46) Li, N. C.; Patrissi, C. J.; Che, G. L.; Martin, C. R. *J. Electrochem. Soc.* **2000**, *147*, 2044.

(47) Eftekhari, A. *Electrochim. Acta* **2001**, *47*, 495.

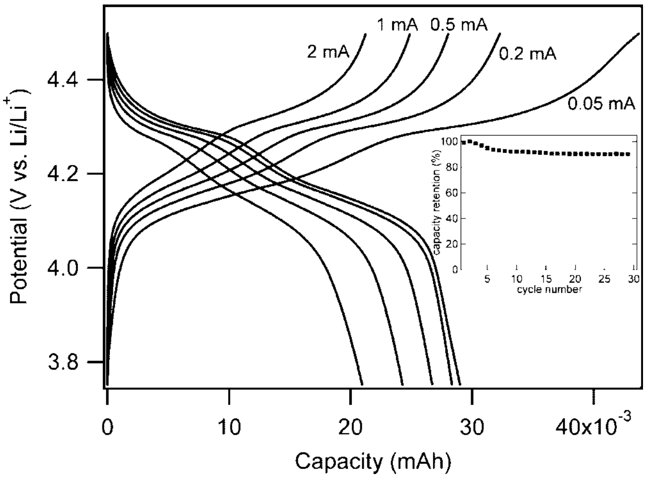

**Figure 10.** Charge and discharge profiles of a 3DOM $LiMn_2O_4$ electrode in a 9 M $LiNO_3$ aqueous solution, measured at various rates, indicated for the charging curves. Currents with same values and opposite signs were applied for the corresponding discharge profiles. In the inset is reported the relative discharge capacity for the first 30 cycles recorded at 20 $\mu$A.

the upper limit for galvanostatic charge−discharge has been set to 4.45 V.

Charge and discharge curves at different rates are shown in Figure 10. At the lowest rates, the capacity during charging appears larger than during discharge; we attribute this difference, which tends to zero at higher rates, to a parasitic process such as water oxidation.[28] At low rates, discharge capacity increases, while charge capacity tends to a maximum value. Thus, we estimate C rates from the highest discharge capacity measured. By dividing the applied current by this capacity, 50 $\mu$A corresponds to about 1.8 C and 2 mA to 70 C. At the highest rates, capacity values are smaller, but two potential plateaus are still observed, in good agreement with cycling voltammograms. The original capacity is recovered if a lower rate is applied. Capacity loss over 30 discharge cycles at a rate of 20 $\mu$A is reported in the inset of Figure 10. Capacity stabilizes at 90% of the initial value, and we observed no significant changes in the shape of the profiles. Accordingly, we could not notice any sign of deterioration comparing SEM images before and after the electrochemical study. The open framework of an inverse opal sustains very well the volume changes produced during the insertion–deinsertion cycles. Good cycle life has been reported also in cases of mesoporous[48] and nanotubular[28] $LiMn_2O_4$ or 3DOM $Li_4Ti_5O_{12}$.[17] Poorer cyclability that has been reported with 3DOM $SnO_2$[16] and $LiCoO_2$[14] may originate from particle−particle disconnections due to compound-specific properties, such as much higher volume changes or poorly sintered grain boundaries.[14]

These results show that the inverse opal $LiMn_2O_4$ displays a high rate capability and good cycle stability. The rate capabilities compare well with those obtained by Martin and co-workers on nanotubular $LiMn_2O_4$ electrodes,[28] and to our knowledge are among the highest reported in literature. A systematic study of the effects of the macroporous structure on the electrode performance will be published elsewhere.

## Conclusions

In this work, colloidal templating methods have been used to prepare porous networks of nanocrystalline $LiMn_2O_4$. Intermediate reaction products formed when nitrates are used as precursors seem to play a key role in stabilizing the inorganic skeleton during the elimination of the template. Below 100 °C, nitrates first oxidize Mn(II) to form $Mn_2O_3$, which proves to be sufficiently rigid to form 3DOM materials that retained the shape of the template when this becomes fluid. Between 150 and 350 °C, most Mn is converted to $MnO_2$. Finally, around 400 °C Li reacts with $MnO_2$ to form spinel $LiMn_2O_4$. At higher temperatures, direct conversion of $Mn_2O_3$ to $LiMn_2O_4$ and elimination of structural disorder in $LiMn_2O_4$ were observed. Adsorption results suggest that nanocrystals are closely packed and sintered favoring the use of this material in electrochemical applications. The electrochemical behavior of prepared materials has been studied without making use of additives, showing a high reversibility in inserting/deinserting lithium over a large number of cycles. The rates that can be applied without dramatic capacity loss are among the highest reported in the literature.

**Acknowledgment.** We wish to thank Dr. Rosa Rojas López and Dr. José Manuel Amarilla Alvarez for fruitful discussions, Prof. Eduardo Ruiz-Hitzky for providing access to his electrochemical testing facility, and the Spanish Ministry for Education and Science (Contract MAT2004-03070-C05 and Programa Ramón y Cajal, D.T.) and the Autonomous Community of Madrid (Contract S-0505/PPQ/0358) for financial support.

**Supporting Information Available:** TG/DTA analysis of impregnated opals in air and SEM images of large areas of monoliths (PDF). This material is available free of charge via the Internet at http://pubs.acs.org.

CM702134S

---

(48) Luo, J. Y.; Wang, Y. G.; Xiong, H. M.; Xia, Y. Y. *Chem. Mater.* **2007**, *19*, 4791.